



OPEN ACCESS

EDITED BY

Naurang Saini,
Sapienza University of Rome, Italy

REVIEWED BY

Aditya Sharma,
University of Petroleum and Energy Studies,
India
Raphaela De Oliveira,
Brazilian Synchrotron Light Laboratory, Brazil

*CORRESPONDENCE

C. R. Dean,
✉ cd2478@columbia.edu
V. Bisogni,
✉ bisogni@bnl.gov
K. W. Plumb,
✉ kemp_plumb@brown.edu

RECEIVED 07 February 2025

ACCEPTED 14 May 2025

PUBLISHED 25 June 2025

CITATION

DiScala MF, Hsieh V, Jessen BS, Gu Y, Rizzo DJ, Amontree JM, Yan X, Wang Q, Kapfer M, Kim T, Geiwitz M, Natale G, Pellicciari J, Hone JC, Burch KS, Basov DN, Dean CR, Bisogni V and Plumb KW (2025) Characterizing sample degradation from synchrotron based X-ray measurements of ultra-thin exfoliated flakes. *Front. Electron. Mater.* 5:1572940. doi: 10.3389/femat.2025.1572940

COPYRIGHT

© 2025 DiScala, Hsieh, Jessen, Gu, Rizzo, Amontree, Yan, Wang, Kapfer, Kim, Geiwitz, Natale, Pellicciari, Hone, Burch, Basov, Dean, Bisogni and Plumb. This is an open-access article distributed under the terms of the [Creative Commons Attribution License \(CC BY\)](https://creativecommons.org/licenses/by/4.0/). The use, distribution or reproduction in other forums is permitted, provided the original author(s) and the copyright owner(s) are credited and that the original publication in this journal is cited, in accordance with accepted academic practice. No use, distribution or reproduction is permitted which does not comply with these terms.

Characterizing sample degradation from synchrotron based X-ray measurements of ultra-thin exfoliated flakes

M. F. DiScala¹, V. Hsieh², B. S. Jessen², Y. Gu³, D. J. Rizzo², J. M. Amontree⁴, X. Yan⁴, Q. Wang¹, M. Kapfer², T. Kim³, M. Geiwitz⁵, G. Natale⁵, J. Pellicciari³, J. C. Hone⁴, K. S. Burch⁵, D. N. Basov², C. R. Dean^{2*}, V. Bisogni^{3*} and K. W. Plumb^{1*}

¹Department of Physics, Brown University, Providence, RI, United States, ²Department of Physics, Columbia University, New York, NY, United States, ³National Synchrotron Light Source II, Brookhaven National Laboratory, Upton, NY, United States, ⁴Department of Mechanical Engineering, Columbia University, New York, NY, United States, ⁵Department of Physics, Boston College, Chestnut Hill, MA, United States

It is undeniable that novel 2D devices and heterostructures will have a lasting impact on the advancement of future technologies. However, the inherent instability of many exfoliated van der Waals (vdW) materials is a well-known hurdle yet to be overcome. Thus, the sustained interest in exfoliated vdW materials underscores the importance of understanding the mechanisms of sample degradation to establish proactive protective measures. Here, the impact of prolonged synchrotron-based X-ray beam exposure on exfoliated flakes of two contemporary vdW materials, NiPS₃ and α -RuCl₃, is explored using resonant inelastic X-ray scattering (RIXS) and total fluorescence yield X-ray absorption spectroscopy (XAS). In NiPS₃, the resulting RIXS and XAS spectra show a suppression, then vanishing, of NiS₆ multiplet excitations coupled with an upward shift of the peak energy of the XAS as a function of X-ray dose. In α -RuCl₃, the signs of beam damage from the RIXS spectra are less evident. However, the post-experiment characterization of both materials using Raman spectroscopy exhibits signals of an amorphous and disordered system compared to pristine flakes; in addition, energy-dispersive X-ray spectroscopy of NiPS₃ shows evidence of ligand vacancies. As synchrotron radiation is fast becoming a required probe to study 2D vdW materials, these findings lay the groundwork for the development of future protective measures for synchrotron-based prolonged X-ray beam exposure, as well as for X-ray free electron laser.

KEYWORDS

resonant inelastic soft X-ray scattering (RIXS), 2D magnetism, magnetism, prospects, van der Waals (vdW), NiPS₃, RuCl₃, graphene

1 Introduction

Advancements in the fabrication of 2D magnetic van der Waals (vdW) materials have largely been driven by the potential to reveal unique magnetic states not achievable in three dimensions, and the possibility of engineering new magnetic phases through extrinsic perturbations, such as stacking (Park, 2016; Sivadas et al., 2018; Gong et al., 2017; Tang et al., 2023). Such progress is crucial for the production of future magnetic based spintronic

devices (Hellman et al., 2017; Burch et al., 2018). The first steps towards this goal however, requires a comprehensive picture of a materials magnetic properties, which necessitates understanding the propagation of spin-waves.

The momentum and energy-resolved magnetic excitation spectra in bulk materials are readily measured by inelastic neutron scattering (INS) or resonant inelastic X-ray scattering (RIXS). However, the extremely small sample volumes of 2D magnetic materials make INS not feasible. Optical measurements can be used to obtain some information about the magnetic excitations in 2D materials, but are limited to negligible momentum transfers so can only provide limited information of magnetic excitations in antiferromagnets. Hence, X-ray scattering techniques are essential for advancing our understanding of 2D magnetism (Ahn et al., 2024).

Sample degradation has been a persistent problem in the fabrication of clean, few-layer vdW materials. A primary source of degradation is the physical adsorption of oxygen on the surface, or the chemisorption of oxygen into ligand vacancies (Grünleitner et al., 2022; Wu et al., 2021). Extensive research has been conducted on methods to protect exfoliated flakes from degradation in ambient atmosphere. These predominantly involve the placement of a capping layer of hBN or thin-films such as Al_2O_3 (Li Q. et al., 2019) on top of the 2D material. However, during an X-ray or light scattering experiment, large quantities of energy are potentially deposited into the 2D material, and in this case, it is also possible that the measurements damage or degrade the sample quality. For instance, light induced sample damage has been reported when conducting Raman measurements on exfoliated flakes, even when using low powers (Sandilands et al., 2010; Kuo et al., 2016; Kim et al., 2019). So far, little is known about how such damage occurs or about the robustness of any protections against such effects.

In this work, we demonstrate the X-ray induced generation of ligand vacancies using a combination of resonant inelastic X-ray scattering (RIXS) and X-ray absorption spectroscopy (XAS) in two contemporary magnetic vdW materials, NiPS_3 and $\alpha\text{-RuCl}_3$, including both bare and graphene capped $\alpha\text{-RuCl}_3$, each studied for their potentially unique 2D magnetism. NiPS_3 has emerged as a highly promising material for studying the XY model in a real 2D system, while $\alpha\text{-RuCl}_3$ is recognized as a prime candidate to host the long-sought Kitaev quantum spin-liquid state in 2D (Kim et al., 2019; Sarikurt et al., 2018; Kim et al., 2022). Prolonged exposure to intense X-ray beams that is necessary to carry out RIXS measurements was found to result in significant degradation of both samples.

The RIXS spectra of NiPS_3 show transient multiplet excitations and a transition towards predominantly fluorescence-like excitations as a function of X-ray dosage, which is reflected in the disappearance of majority multiplet excitation peaks in the XAS spectra. On the other hand, degradation of $\alpha\text{-RuCl}_3$ was only observed and characterized post RIXS measurements.

Post-irradiation EDS analysis of NiPS_3 revealed a reduction in sulfur and phosphorus when compared to a pristine sample, and increased levels of chemisorbed oxygen. Additionally, Raman spectra of both materials were indistinguishable from the Si substrate apart from a tapering background. These results are consistent with X-ray induced ligand expulsion and a significant

crystallographic reorganization. These results emphasize the requirement for developing more robust and specialized sample protection techniques in light of the necessity for synchrotron based X-ray scattering to explore dispersive magnetic excitations in the 2D limit of exfoliated flakes, and especially for novel heterostructure devices.

2 Materials and methods

Single crystal samples of NiPS_3 were grown by vapor transport, following previously published methods (Wildes et al., 2015; Lançon et al., 2018; DiScala et al., 2024; See supplementary material for details) (See Table. SI for more details). NiPS_3 crystallizes in the monoclinic $C2/m$ space group with Ni ($S = 1$) atoms on honeycomb lattices in the ab -planes. Each Ni atom is octahedrally coordinated by 6 S atoms, with P atoms situated between the 2D sheets of NiS_6 that form the vdW gap along the c -axis with an interlayer spacing of ≈ 0.636 nm (Kuo et al., 2016; Wildes et al., 2015). NiPS_3 magnetically orders at a transition temperature of $T_N = 155$ K, forming ferromagnetic zig-zag chains with moments parallel to the a -axis and antiferromagnetically coupled along the b -axis, along with a small out of plane component (Wildes et al., 2015; Wildes et al., 2022).

To prepare NiPS_3 samples for RIXS measurements, bulk crystals were exfoliated using conventional scotch-tape methods (Kuo et al., 2016), deposited onto Polydimethylsiloxane (PDMS), and then transferred to Si substrates pre-patterned with Au fiducial markers, as seen in Supplementary Figure S1a. The Au fiducial markers provide a fluorescence contrast to the Si substrate that allows for unambiguous location of few layer samples whose signals were weak under an X-ray beam (DiScala et al., 2024; See supplementary material for details; Lupascu et al., 2012). Lastly, to protect from ambient air exposure, samples were coated with 3 nm thick Al_2O_3 using electron beam sputtering deposition. At this thickness, the Al_2O_3 capping layer is transparent to X-rays at the Ni L_3 edge. Exfoliation and PDMS transfer were performed in ambient air; within 1 hour of exfoliation, ideal samples were identified and transferred onto Si-substrates, then stored under vacuum and in an argon-filled glovebox until the Al_2O_3 capping layer was deposited. Post deposition, samples were returned to vacuum storage in an argon-filled glovebox. Optical contrast between sample and PDMS was used to determine sample layer count. The optical contrast on PDMS was determined using a combination of previously determined atomic-force microscope thickness measurements and optical contrast with SiO_2 substrate (DiScala et al., 2024). The thickness of the irradiated sample was determined to be ~ 20 layers (L), or ~ 12.72 nm.

To avoid stoichiometric variation between samples, pristine exfoliated samples used as a baseline for the various characterization techniques explored were exfoliated from the same bulk NiPS_3 as the X-ray irradiated sample. These samples were prepared following the aforementioned exfoliation process, but then transferred onto Si/ SiO_2 substrates for further confirmation of sample thickness. Of these samples, one was left in air to test the effect of oxygen and water adsorption on exfoliated samples, while the other was kept under vacuum and stored in an argon-filled glovebox along with the X-ray irradiated sample; this latter sample

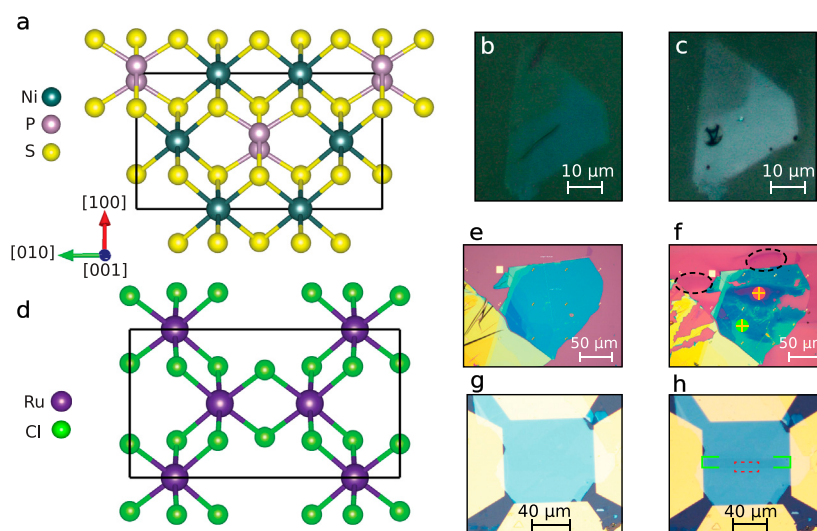


FIGURE 1

(a, d) Crystal structure of NiPS_3 (a) and $\alpha\text{-RuCl}_3$ (d) and orientations on substrate, as shown in the microscope images. (b, c) Microscope images of NiPS_3 pre- (b) and post-irradiation (c). Microscope images of ~ 22 nm $\alpha\text{-RuCl}_3$ before (e) and after (f) X-ray beam exposure. Dashed black circles in (b) mark regions of X-ray induced SiO_2 substrate damage. Red and green circles in (f) mark the *on* and *off* X-ray beam spots for the Raman spectra shown in Figure 8. Microscope images of the G/ RuCl_3 heterostructure before (g) and after (h) X-ray beam exposure; green brackets in (h) demarcate the beam spot region. The red dashed square marks the Raman map region shown in Figure 9.

was only removed from vacuum when measurements were taken, and immediately placed back under vacuum and in the glovebox afterwards.

$\alpha\text{-RuCl}_3$ crystals were grown by the sublimation of RuCl_3 powder sealed in a quartz tube under vacuum. About 1 g of powder was loaded in a quartz tube of 19 mm in outer diameter, 1.5 mm thick, and 10 cm long. The growth was performed in a box furnace. After dwelling at $1,060^\circ\text{C}$ for 6 h, the furnace was cooled to 800°C at a rate of $4^\circ\text{C}/\text{h}$.

To prepare $\alpha\text{-RuCl}_3$ samples for RIXS measurements, bulk crystals were exfoliated onto a Si/SiO_2 substrate with pre-patterned Cr/Au alignment markers for easier optical identification of sample location. $\alpha\text{-RuCl}_3$ flakes of varying thickness were characterized using optical contrast with the SiO_2 substrate as well as using atomic force microscopy.

To prepare graphene/ $\alpha\text{-RuCl}_3$ heterostructure (G/ RuCl_3) samples, graphene films were transferred onto a Si/SiO_2 substrate containing varying thicknesses of exfoliated and pre-characterized $\alpha\text{-RuCl}_3$ crystals. The graphene films grown on Cu foils (Graphene Supermarket) were transferred using the conventional wet transfer method (Suk et al., 2011). The graphene was spin-coated with a thin layer of polymethyl methacrylate (495 PMMA A4 from Kayaku, 4,000 rpm, 1 min, bake at 180°C , 5 min) to provide mechanical support for the transfer. The backside graphene was removed by O_2 plasma for a duration of 1 minute at 100 W. The PMMA/graphene was detached from the copper by placing the sample in copper etchant (Ammonium persulfate $(\text{NH}_4)_2\text{S}_2\text{O}_8$) for 2 h. After washing with DI water 3x, the floating PMMA/graphene layer was transferred to the Si/SiO_2 substrate and dried in vacuum (1 Torr) overnight. Next, the sample was heated on a hot plate at 80°C for 20 min and 180°C for 20 min in an ambient environment. Finally, the sample was soaked in acetone for 30 min, rinsed with IPA, and dried with N_2 . All RuCl_3 samples were prepared and characterized in

air, with no additional precautions taken during the preparation of the G/ RuCl_3 heterostructures with the wet transfer process due to the literature-reported stability of RuCl_3 in air (Zhou et al., 2019). Raman after the wet-transfer process confirms that ambient oxygen and humidity did not affect the quality of either the bare RuCl_3 or the G/ RuCl_3 heterostructures, consistent with the findings in Refs. (Zhou et al., 2019; Breitner et al., 2023). While Breitner et al. perform heat treatment on RuCl_3 in an inert environment, they demonstrate that clear signatures of sample degradation only appear for annealing temperatures beyond 300°C , temperatures which we do not approach in our sample preparation process.

All G/ RuCl_3 heterostructure samples, and some of the $\alpha\text{-RuCl}_3$ flakes, were coated with 10 nm thick Al_2O_3 , using atomic layer deposition in a Cambridge Nano Tech S200. Using electron beam lithography and evaporation, these samples were then patterned with Au markers, as shown in Figures 1e–h, for easier identification of sample location optically and with X-ray fluorescence, in addition to helping heat dissipate from the beam. To do so, samples were spun with a bilayer resist of 950k and 495k PMMA, at 50 nm and 200 nm, respectively. Electron beam exposure was done at 80 kV with a current of 10 nA, and the sample was subsequently developed in a 5°C solution of IPA: H_2O (3:1). Cr/Au (3/50 nm) was then deposited, and the samples were subsequently immersed in acetone for metal lift-off. Samples were then stored at ambient pressure in a nitrogen-filled dry box.

RIXS and XAS measurements were carried out on the SIX 2-ID beamline of the National Synchrotron Light Source II (Dvorak et al., 2016). For NiPS_3 , horizontal scattering geometry was set to $2\theta = 90^\circ$ and sample angle $\theta_m = 77.5^\circ$. RIXS spectra at Ni L_3 edge were collected in 20 min segments using linear vertical polarization with an ≈ 28.8 meV energy resolution (full width at half max, FWHM), after which XAS spectra were collected. Incident X-ray energies varied between 852.6–853.2 eV; with $\sim 10^{12}$ photons/s and a beam

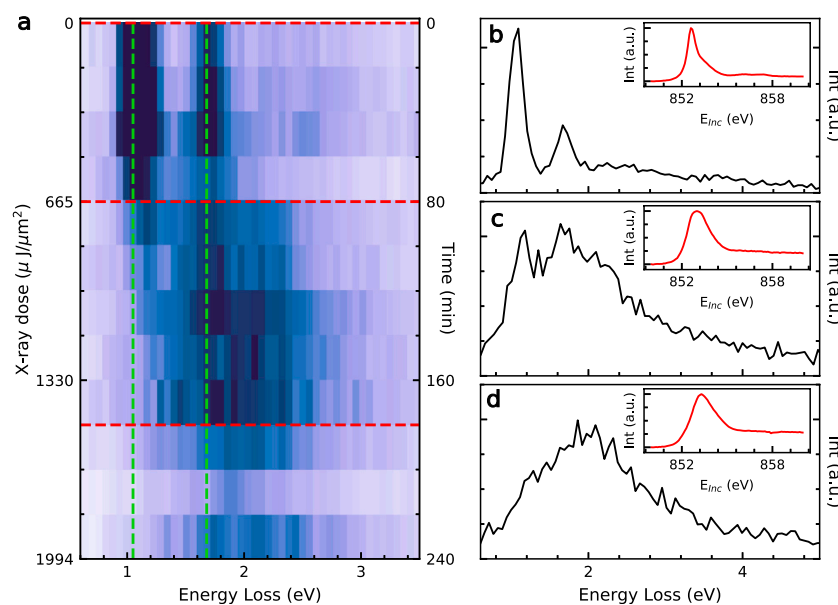


FIGURE 2
(a) Evolution of NiS_6 multiplet excitations irradiation dose (left) and time (right). Changes in spectra are immediately apparent after 20 min of irradiation ($\sim 171 \mu\text{J}/\mu\text{m}^2$), however, multiplet excitations only vanish after more than 80 min of irradiation ($\sim 683 \mu\text{J}/\mu\text{m}^2$). Horizontal dashed red lines indicate the selected RIXS scans of **(b–d)** along with respective XAS spectra shown in insets. Vertical green lines indicate the centroid positions of the first two multiplet excitations.

spot size of $15 \mu\text{m}$ (H) \times $1.7 \mu\text{m}$ (V) (focused by an ellipsoidal mirror placed after the monochromator exit slit), resulting X-ray dosage at the Ni L_3 -edge is $\sim 8.3 \mu\text{J}/\mu\text{m}^2\text{s}$. Bulk NiPS_3 spectra were collected with an identical scattering angle, but in specular geometry, and with an ~ 55.1 meV overall energy resolution FWHM. Sample orientation and structure are shown in [Figure 1a](#), with the c -axis along the direction of the incident beam. Microscope images of NiPS_3 pre- and post-irradiation are shown in [Figures 1b,c](#).

For $\alpha\text{-RuCl}_3$, horizontal scattering geometry was set to $2\theta = 90^\circ$. RIXS spectra were collected for one and a half hours each at three incident energies across the Ru M_3 edge, using linear horizontal polarization, with ≈ 67 meV of energy resolution (full width at half max, FWHM). Incident X-ray energies varied between 460.7 and 465 eV; with $\sim 8 \cdot 10^{12}$ photons/s and a projected beam spot size of $58 \mu\text{m}$ (H) \times $8.3 \mu\text{m}$ (V) ($\theta_{in} = 15^\circ$) and $20.2 \mu\text{m}$ (H) \times $8.3 \mu\text{m}$ (V) ($\theta_{in} = 48^\circ$), resulting X-ray dosages at the Ru M_3 -edge are $\sim 1.58 \mu\text{J}/\mu\text{m}^2\text{s}$ and $4.5 \mu\text{J}/\mu\text{m}^2\text{s}$, respectively. In the following, we will present the RIXS data taken at one excitation energy, coinciding with the maximum of the Ru M_3 edge. Sample orientation and structure are shown in [Figure 1a](#), with the c -axis along the direction of the incident beam. Microscope images of $\alpha\text{-RuCl}_3$ and G/RuCl_3 , pre- and post-irradiation, are shown in [Figures 1e–h](#).

For NiPS_3 , Raman measurements were conducted on a pseudo-confocal Raman microscopy spectrometer (TriVista CRS³) at room temperature in an Argon atmosphere, with an excitation wavelength of 633 nm, excitation power ≤ 1 mW, and spectrometer grating of 1,500 lines/mm. EDS measurements were conducted using a Thermo Scientific Quattro S using a 20 kV accelerating voltage. For $\alpha\text{-RuCl}_3$, Raman measurements were conducted using a Renishaw inVia micro-Raman spectrometer at room temperature in ambient air, with an excitation wavelength of

532 nm, excitation power ≤ 2 mW, and spectrometer grating of 1800 lines/mm.

3 Results

3.1 NiPS_3

[Figure 2A](#) shows the evolution of the first two NiS_6 multiplet excitations, centered at $E_{\text{loss}} = 1.05$ eV and 1.68 eV respectively, as a function of X-ray beam dosage and exposure time. [Figure 2b](#) shows the characteristic NiPS_3 RIXS spectrum at $t = 0$ min (t_0), along with its respective XAS spectrum shown in the inset. These two multiplet excitations are clearly resolved up to $t = 60$ min (t_3). At $t = 80$ min ([Figure 2c](#)) signatures of these two peaks can still be seen, however, superimposed by a large background. Additionally at this time, the XAS spectrum shows the first qualitative change, transitioning from a clear two-peak structure to a single peak, and shifting upwards in incident energy by ≈ 200 meV. As X-ray beam dosage increases, the two multiplet excitations vanish into the electron-hole continuum. Concurrently, the XAS peak continues to shift upward in incident energy, plateauing at $E_{\text{mc}} \approx 853.2$ eV ([Figure 2d](#)). The full time evolution of RIXS and XAS are shown in the Supplementary Materials ([Supplementary Figures S2–4](#)) (See [Supplementary Material](#) for details).

In order to elucidate the affect of prolonged X-ray beam exposure, we begin our analysis with the time/dosage dependent XAS signal. At t_0 we find that four Voigt profiles are required to fit the data, as shown in [Figure 3a](#). The peaks labeled *A* and *B* correspond to the white-line, while SP_1 and SP_2 represent the satellite peaks (Kim et al., 2018; He et al., 2024). As X-ray beam

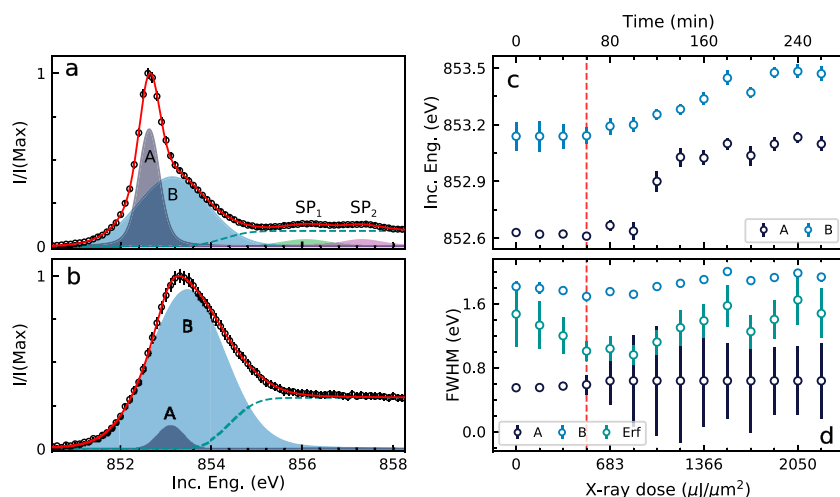


FIGURE 3
 $t = 0$ min **(a)** and $t = 260$ min **(b)** NiPS₃ XAS spectra at Ni L₃-edge. Black points are experimental data and red lines show total fit to the data using four Voigts **(a)** and two Voigts **(b)** along with an error step function. **(c)** Centroid positions of A and B with irradiation dosage (bottom) and time (top). Vertical dashed red line demarcates the last time both satellite peaks were reliably fit before vanishing into background, corresponding to $\sim 512 \mu\text{J}/\mu\text{m}^2$. **(d)** Evolution of the FWHM of peaks A and B, and of the step error function, with irradiation dosage and time. Vertical dashed red lines again demarcate the vanishing of the satellite peaks.

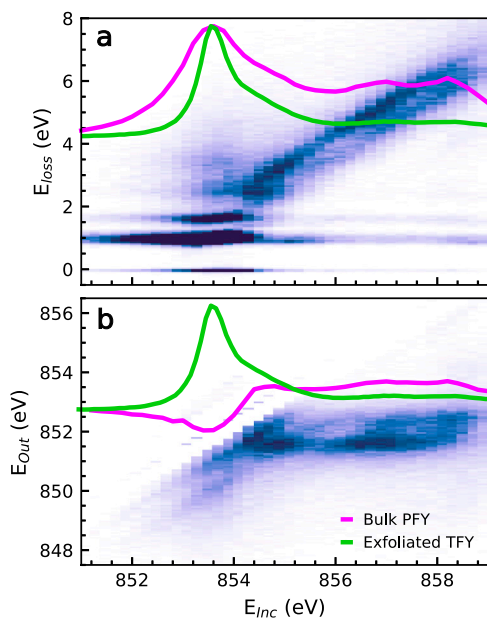


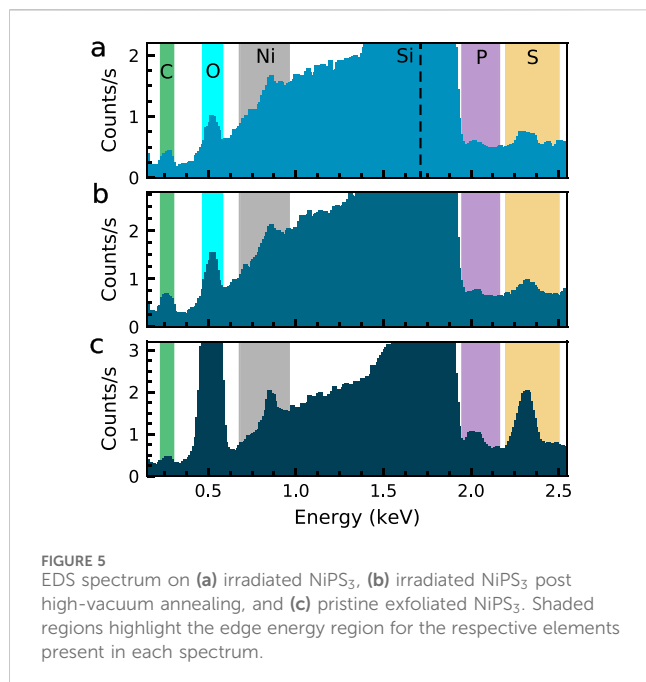
FIGURE 4
 Bulk NiPS₃ RIXS map shown as functions of incident energy (E_{inc}) vs energy loss (E_{loss}) **(a)** and E_{inc} vs outgoing energy (E_{out}) **(b)**. Both maps are also shown with their respective PFY spectra and the exfoliated NiPS₃ XAS. The XAS white-line has been shifted to coincide with the PFY white-line. The RIXS map in **(b)** has had the elastic line and first two multiplet excitations removed, which is reflected in the intensity dip in the PFY. The PFY after excitation subtraction was normalized to the maximum of the PFY prior to subtraction.

exposure continues, both peaks A, SP₁, and SP₂ decrease intensity, and after t_3 , SP₁ and SP₂ vanish into the background. Simultaneously, peak A nearly reached its minimum intensity

and was significantly overlapped by the fit of peak B, causing the XAS to assume a seemingly one-peak structure (inset of Figures 2b,c and Figure 3b). However, from $t \geq t_3$, the best fits minimizing the residuals were still achieved with two peaks (Supplementary Figure S3). As seen in Figure 3c, from $t = 0 \rightarrow 260$ min, peak A shifts upwards in incident energy by 470 ± 40 meV. During the same time frame, peak B only shifts upwards in incident energy by 331 ± 83 meV, with an average $\Delta E_{inc} = 25 \pm 18$ meV. Notably, the FWHM of peak B stayed fairly constant, averaging 1.85 ± 0.01 eV across the full time range measured (Figure 3d). The change in FWHM of peak A, however, is not so readily gleaned after t_3 as discussed in the full fitting procedure found in the Supplementary Material (See supplementary material for details).

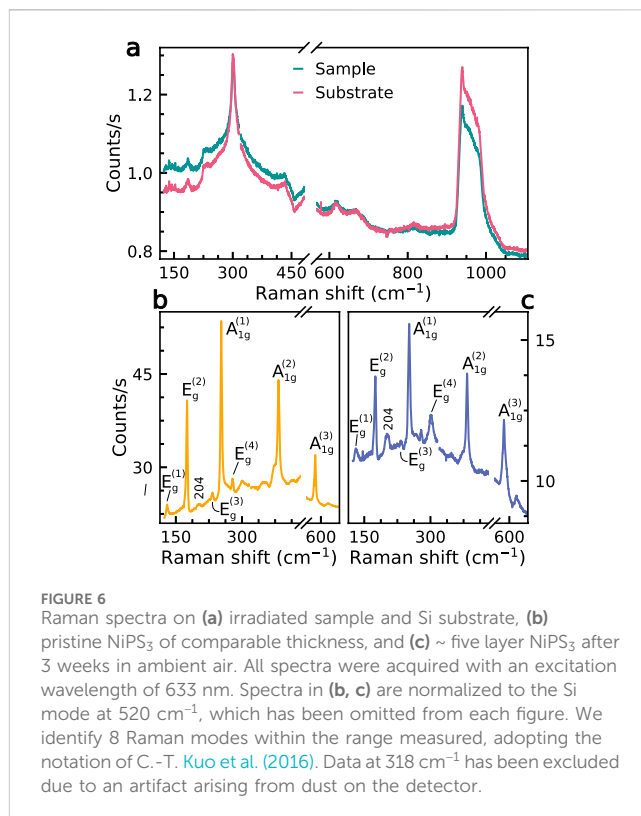
Using the bulk NiPS₃ RIXS map, shown in Figure 4, we are able to disentangle the origin of each feature in the XAS. Figure 4a shows RIXS map function of incident energy (E_{inc}) vs energy loss (E_{loss}). Features of constant E_{loss} are Raman-like excitations and have been previously characterized as multiplet excitations (DiScala et al., 2024; He et al., 2024), while the sloped features are fluorescence excitations (Ament et al., 2011). We then find great agreement between the exfoliated XAS at t_0 compared to the partial fluorescence yield (PFY), defined as the sum of E_{loss} values for each E_{inc} in the RIXS map. Figure 4b then shows the RIXS map as a function of E_{inc} vs outgoing energy (E_{out}) in order to highlight the constant outgoing energy of the fluorescence excitations. By subtracting the elastic line and first two NiS₆ multiplet excitations from the RIXS map in Figure 4b, we again compare the XAS and PFY and find that the majority of the intensity within the region of peak B is associated with fluorescence excitations.

To better understand the effects of X-ray induced sample degradation, we performed a suite of sample characterization experiments and compared results with pristine flakes of comparable thickness. Figure 5 shows the elemental EDS mapping of the irradiated NiPS₃ (Figure 5a) compared to a



pristine sample (Figure 5c). The irradiated NiPS₃ shows significantly less sulfur when compared to the pristine sample and, additionally, increased levels of carbon and oxygen. The oxygen is not associated with the substrate or Al₂O₃ capping layer, as evidenced by the EDS spectrum of the neighboring Si substrate, which showed lower oxygen levels than the sample and substrate combined (see Supplementary Figure S5 in (See Supplementary Material for details)). We note again that the pristine NiPS₃ sample was exfoliated on an SiO₂ substrate, and thus, the oxygen in Figure 5c arises from the substrate alone. The presence of carbon on the sample can be explained by the outgassing of carbon from stainless steel in ultra-high vacuum (Calder and Lewin, 1967; Nevshupa and de Segovia, 2002; Ashraf et al., 2019). Physical adsorption of oxygen is a known source of contamination/ degradation for a variety of exfoliated flakes (Li Q. et al., 2019). However, it has also been suggested that chemisorption of oxygen on exfoliated flakes is possible, especially in the presence of sulfur vacancies, albeit slow in ambient air (Grünleitner et al., 2022; Wu et al., 2021; Liu et al., 2016).

Although removal of adsorbed oxygen on the surface of exfoliated flakes is not widely reported, there is evidence suggesting high-vacuum annealing can expel this adsorbed oxygen (Grünleitner et al., 2022). Thus, we assessed the degree of oxygen passivation of sulfur vacancies through chemisorption on the irradiated sample via high-vacuum annealing at 120°C for 150 min. However, the elemental EDS mapping post-vacuum annealing did not show a reduced oxygen content (Figure 5b), suggestive of chemisorption of oxygen, rather than physical adsorption. By subtracting the EDS spectrum of the substrate alone, it is evident that the excess oxygen in the sample is not associated with Al₂O₃ capping layer. It is then likely that this oxygen originated from the short time frame of moving the sample from the ultra-high vacuum RIXS chamber to the vacuum desiccator; a normally slow process in ambient air sped up by the generation of sulfur vacancies.



It is clear from the EDS analysis that the prolonged, high-flux X-ray beam exposure produced sulfur vacancies in exfoliated flakes of NiPS₃. Despite these vacancies, it is possible that the structure of NiPS₃ stays somewhat intact (Grünleitner et al., 2022). We thus probe the structure of the irradiated sample using Raman spectroscopy with an excitation wavelength of 633 nm, again comparing to a pristine sample of comparable thickness. Figure 6a shows the Raman spectra of the irradiated sample, taken before high-vacuum annealing, which shows none of the Raman modes indicative of NiPS₃ and appears indistinguishable from the Si substrate apart from a background shift that tapers off beyond the 520 cm⁻¹ Si peak. In contrast, Figure 6b shows the Raman spectrum for the pristine NiPS₃ sample, where we clearly identify the previously reported 8 Raman-active phonon modes in NiPS₃ (3A_{1g} + 5E_g), including the new peak at 204 cm⁻¹ that appears in thin exfoliated flakes (Kuo et al., 2016; Kim et al., 2019; Bernasconi et al., 1988). In addition, we find signals of amorphous carbon in the irradiated NiPS₃ Raman spectra that is absent in the non-irradiated samples (Supplementary Figure S6a). Lastly, we tested the affect of physically adsorbed oxygen on the modulation of Raman modes in exfoliated NiPS₃. Figure 6c shows the Raman spectra of a five layer flake of NiPS₃ left in ambient air for 3 weeks, where all previously reported Raman modes are identifiable. This result indicates that adsorbed oxygen is not responsible for the Raman mode suppression seen in the irradiated sample (Kuo et al., 2016).

3.2 α-RuCl₃

The goal of the α-RuCl₃ measurements was to investigate the electronic evolution in α-RuCl₃ at the interface with graphene (Rizzo

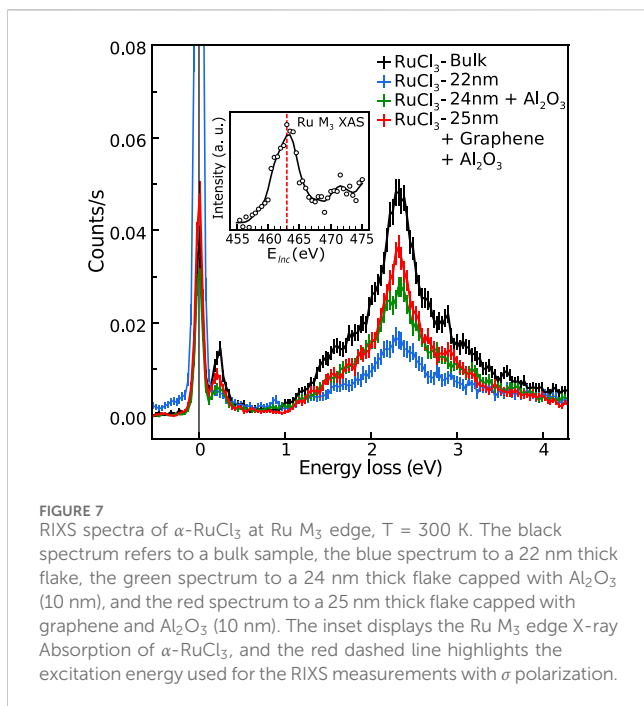


FIGURE 7
RIXS spectra of α -RuCl₃ at Ru M₃ edge, T = 300 K. The black spectrum refers to a bulk sample, the blue spectrum to a 22 nm thick flake, the green spectrum to a 24 nm thick flake capped with Al₂O₃ (10 nm), and the red spectrum to a 25 nm thick flake capped with graphene and Al₂O₃ (10 nm). The inset displays the Ru M₃ edge X-ray Absorption of α -RuCl₃, and the red dashed line highlights the excitation energy used for the RIXS measurements with σ polarization.

et al., 2020; Wang et al., 2020). A thin layer of α -RuCl₃ was preferred to enhance the contrast of the interface effect. Therefore, we first investigated several samples of α -RuCl₃ with variable thicknesses from, 100 nm (bulk) down to 7 nm, to explore possible changes in the electronic structure occurring due to the reduced number of layers (DiScala et al., 2024). For this step, we considered bare flakes of α -RuCl₃, and flakes capped with Al₂O₃ and framed by gold markers. Next, we investigated heterostructures (G/RuCl₃) made by stacking α -RuCl₃, graphene, and Al₂O₃, ultimately framed by gold markers.

In Figure 7, we present the bulk Ru M₃ RIXS data compared to spectra obtained from α -RuCl₃ flakes of an intermediate thickness range (22–25 nm), chosen as a representative case. All spectra were measured with the same scattering geometry ($\theta_{in} = 15^\circ$ and $2\theta = 90^\circ$) and at the same excitation energy, main peak of the Ru M₃ XAS (see inset in Figure 7). The bulk RIXS spectrum is in good agreement with previous studies (Lebert et al., 2020). The RIXS spectrum measured on a 22 nm bare flake of α -RuCl₃ presents the overall same features observed in the bulk, but with reduced intensity and a strongly enhanced elastic line. The green and the red RIXS spectra in Figure 7 refer to the Al₂O₃ capped α -RuCl₃ flake (24 nm) and to the heterostructure α -RuCl₃ (25 nm)/graphene/Al₂O₃, respectively. These spectra present similar intensity: they are weaker than the bulk signal, but stronger than the signal from the 22 nm flake. Their elastic lines are also comparable with the one from the bulk. The intensity variation obtained between these RIXS spectra opens the question whether the effect is intrinsic to the physics of the samples or caused by beam damage. For this reason, a post-characterization investigation was performed on all samples, including optical microscope images and Raman spectroscopy.

Post-irradiation characterization of bare α -RuCl₃ suggests that sample degradation due to X-ray beam exposure is remarkably similar to that of NiPS₃. The Raman spectra of irradiated

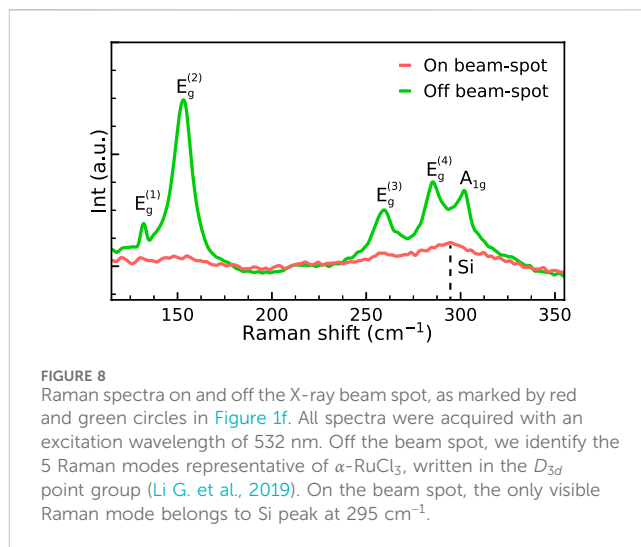


FIGURE 8
Raman spectra on and off the X-ray beam spot, as marked by red and green circles in Figure 1f. All spectra were acquired with an excitation wavelength of 532 nm. Off the beam spot, we identify the 5 Raman modes representative of α -RuCl₃, written in the D_{3d} point group (Li G. et al., 2019). On the beam spot, the only visible Raman mode belongs to Si peak at 295 cm⁻¹.

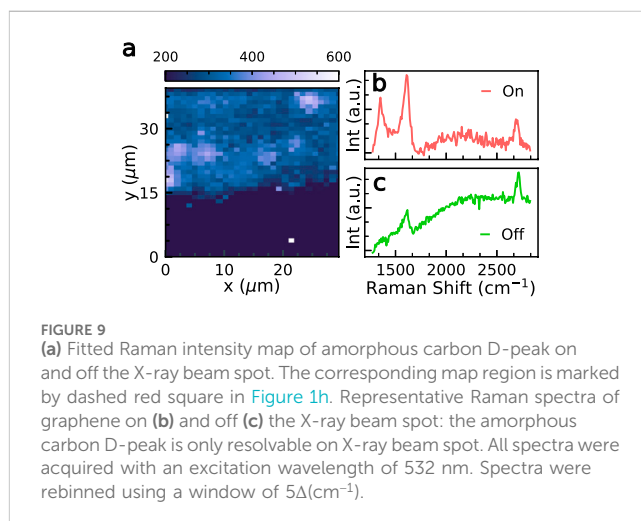


FIGURE 9
(a) Fitted Raman intensity map of amorphous carbon D-peak on and off the X-ray beam spot. The corresponding map region is marked by dashed red square in Figure 1h. Representative Raman spectra of graphene on (b) and off (c) the X-ray beam spot: the amorphous carbon D-peak is only resolvable on X-ray beam spot. All spectra were acquired with an excitation wavelength of 532 nm. Spectra were rebinned using a window of $5\Delta(\text{cm}^{-1})$.

α -RuCl₃ lacks any visible phonon modes indicative of α -RuCl₃ (Figure 8c). In contrast, the Raman spectra on the non-irradiated region of the sample retains the six characterizing phonon modes of α -RuCl₃ (Figure 8c) (Li G. et al., 2019). As was the case for irradiated NiPS₃ sample, these results are indicative of a drastic structural reorganization of α -RuCl₃ due to irradiation. In addition, we find traces of amorphous carbon in the Raman spectra of bare α -RuCl₃, on and off the beam-spot (Supplementary Figure S7b). The presence of amorphous carbon off the beam-spot originates from the X-ray beam rastering process used for sample localization.

Interestingly, signs of substrate damage can be seen when comparing the optical microscope images of bare α -RuCl₃ before (Figure 1e) and after irradiation (Figure 1f, black dashed circles). Optical contrast is a powerful tool to quickly and reliably determine the thickness of ultra-thin exfoliated flakes (Ivanova et al., 2024); a prerequisite of reliable optical contrast measurements is a nominally uniform SiO₂ layer beneath the sample. However, if irradiation alters the uniformity of the SiO₂ layer, then optical contrast would no longer be a reliable determinant of sample thickness.

Similar optical indications of sample damage were seen on the G/RuCl₃ heterostructure, as displayed in Figure 1g (before) and Figure 1h (after, demarcated by green brackets). Herein, we explore the sample degradation of the graphene capping layer due to the prolonged irradiation. Figure 9c shows a spatial map of the carbon D-peak (1,350 cm⁻¹) fitted intensity extracted from Raman measurements. The mapped area is demarcated by a dashed red box in Figure 9b, and it spans across a beam irradiated area and a non-irradiated area. Figures 9d,e show characteristic Raman spectra measured on and off the irradiated region, respectively. Both spectra display characteristic graphene peaks, the G-peak (1,580 cm⁻¹) and the 2D-peak (2,690 cm⁻¹); whereas the D-peak is only visible in the spectra collected within the irradiated area (Figure 9d) and is a fingerprint of amorphous carbon (Saito et al., 2011). Additionally, fitting the intensity of the G-peak and 2D-peak across the scanned area resulted in an intensity ratio of (I_{2D}/I_G) \approx two in the non-irradiated region and a ratio of ≤ 0.5 in the irradiated region: this ratio is representative of low and high levels of disorder in graphene, respectively (Saito et al., 2011; Kim et al., 2009).

4 Discussion

The EDS analysis on NiPS₃ clearly indicates the expulsion of sulfur and phosphorus due to X-ray beam exposure. Yet, simply creating ligand vacancies does not tell the complete story of the extent of sample degradation. Ligand vacancies are naturally present in exfoliated samples, however the transience of multiplet excitations in the RIXS spectra, and the majority multiplet peaks in the XAS spectra (*A*, SP₁, SP₂) are indicative of a more severe structural reorganization. Density functional theory (DFT) calculations on NiPS₃ with \approx 5% sulfur vacancies found drastic crystallographic and electronic structure changes (Wu et al., 2021). In fact, the calculated DOS of monolayer NiPS_{3-x} shows two new states; one of mostly S-3*p* character just below E_F, and one of Ni-3*d* character in the energy gap above E_F. These results are consistent with our RIXS spectra which showed progressively favorable fluorescence excitations with increasing sulfur vacancy generation.

The Raman spectra on the irradiated NiPS₃ sample further substantiate the claim of drastic crystallographic structure changes due to ligand vacancies. The lack of visible phonon modes associated with NiPS₃, and the large tapering background that the Si modes sit atop, are suggestive of a disordered system with decoherent modes. In pristine NiPS₃, the modes below 220 cm⁻¹ are dominated by Ni-S, Ni-P, S-S, S-P, and P-P bond bending, while modes above 300 cm⁻¹ are mostly associated with intra-molecular vibrations from the (P₄S₆)⁴⁺ bipyramid (Kim et al., 2019; Bernasconi et al., 1988). While small amounts of sulfur vacancies may lead to modulations in the (P₄S₆)⁴⁺ bipyramidal dominant modes, the absence of the lower cm⁻¹ bond bending dominant modes is again indicative of a more severe structural reorganization.

The connection between the adsorbed oxygen and the absence of visible Raman modes, however, is still not fully understood. C.-T. Kuo et al. have shown that, for a three layer flake of NiPS₃ left in air for 11 days, only remnants of the A_{1g}⁽²⁾ and A_{1g}⁽³⁾ modes are visible (Kuo et al., 2016), implying that adsorbed oxygen has a destructive affect on the modulation of sulfur planes and of the nickel atoms. However, when measuring the Raman spectra of a five layer flake of

NiPS₃ left in air for 3 weeks, we are still able to clearly resolve all reported Raman modes.

For the case of α -RuCl₃, the Raman spectra of the irradiated bare flake show no visible phonon modes associated with crystalline α -RuCl₃, suggesting similar sample damage as was characterized in NiPS₃. Additionally, the spatial D-peak Raman intensity map of G/RuCl₃ clearly depicts a departure from ordered graphene outside of the irradiated region, to disordered graphene, or amorphous carbon, within. The change in I_{2D}/I_G across the boundary of the irradiation region is further indicative of this departure. As previously mentioned, the outgassing of carbon from stainless steel in ultra-high vacuum is a commonly known phenomenon. Thus, a portion of the amorphous carbon within the irradiated area originated from the outgassing process, while the remainder was generated from the irradiation of the original ordered graphene. However, as no signatures of amorphous carbon were observed in the Raman spectra outside the irradiated region, it is reasonable to assume that most of the amorphous carbon observed within the irradiated region originates from the structural disorder of the graphene caused by the X-ray beam exposure. Based on this evidence, the RIXS spectra measured on the thin α -RuCl₃ samples were considered non-representative of the pristine systems. Although there was no post-characterization performed on the Al₂O₃ capped α -RuCl₃ flake, the fact that its RIXS spectrum overlapped well with that of the clearly damaged G/RuCl₃ heterostructure brings into question the α -RuCl₃ RIXS measurement quality as well.

The stability of exfoliated flakes is in general quantified by the materials defect generation energy (DGE), often calculated using DFT. (Wu et al., 2021; Hu et al.; Yang et al., 2023). Al₂O₃ capping layers have proven an effective passivation method to prevent oxidation in ambient conditions for a variety of vdW materials (Li Q. et al., 2019; Geiwitz et al., 2024). However, up to 10 nm of Al₂O₃ was unable to prevent sample damage during X-ray beam exposure. Thus, calculations detailing the changes in the DGE of various multilayer/capping layer systems are desirable as they can provide a means of testing various capping layers prior to experimentation.

In summary, we characterized the means of sample degradation due to high-flux synchrotron based X-ray scattering on two contemporary vdW materials, NiPS₃ and α -RuCl₃. RIXS and XAS measurements of NiPS₃ showed transient multiplet excitations as a function of X-ray dosage, while EDS and Raman confirmed the expulsion of sulfur and structural reorganization. Although EDS measurements of post-irradiation α -RuCl₃ is needed to conclusively determine ligand expulsion as the exact means of sample damage, the remarkably similar Raman spectra of α -RuCl₃ and NiPS₃ post-irradiation suggests a consistent degradation route. These results emphasize the necessity for more robust protection techniques for 2D exfoliated flakes beyond ambient conditions, else the novel magnetic prospects these, and other magnetic vdW materials offer will remain unrealized. In addition, we showed evidence of local graphene amorphousization in the irradiated region of G/RuCl₃. This finding is significant for future synchrotron experiments on graphene-based heterostructures, as the structural integrity of graphene is crucial for preserving the emergent phenomenon of these systems. More broadly, our work should stimulate systematic pre- and post-characterization methods of samples, especially when the thickness is reduced and when high-

brilliance X-ray sources are used, including X-ray free electron lasers.

Data availability statement

The raw data supporting the conclusions of this article will be made available by the authors, without undue reservation.

Author contributions

MD: Conceptualization, Data curation, Formal Analysis, Investigation, Methodology, Supervision, Visualization, Writing – original draft, Writing – review and editing. VH: Data curation, Formal Analysis, Methodology, Writing – review and editing. BJ: Data curation, Formal Analysis, Methodology, Writing – review and editing. YG: Data curation, Formal Analysis, Writing – review and editing. DR: Data curation, Writing – review and editing. JA: Data curation, Writing – review and editing. XY: Data curation, Writing – review and editing. QW: Data curation, Writing – review and editing. MK: Data curation, Writing – review and editing. TK: Data curation, Formal Analysis, Writing – review and editing. MG: Methodology, Supervision, Validation, Writing – review and editing. GN: Methodology, Supervision, Writing – review and editing. JP: Investigation, Methodology, Supervision, Writing – review and editing. JH: Funding acquisition, Project administration, Resources, Supervision, Writing – review and editing. KB: Funding acquisition, Project administration, Resources, Supervision, Writing – review and editing. DB: Funding acquisition, Project administration, Resources, Supervision, Writing – review and editing. CD: Funding acquisition, Project administration, Resources, Supervision, Writing – review and editing. VBi: Conceptualization, Data curation, Formal Analysis, Funding acquisition, Investigation, Methodology, Project administration, Resources, Supervision, Writing – review and editing. KP: Conceptualization, Funding acquisition, Investigation, Project administration, Resources, Supervision, Writing – review and editing.

Funding

The author(s) declare that financial support was received for the research and/or publication of this article. Work at Brown University was supported by the National Science Foundation under Grant No. 2429695. The work on α -RuCl₃ was supported

References

- Ahn, Y., Guo, X., Son, S., Sun, Z., and Zhao, L. (2024). Progress and prospects in two-dimensional magnetism of van der Waals materials. *Prog. Quantum Electron.* 93, 100498. doi:10.1016/j.pquantelec.2024.100498
- Ament, L. J. P., van Veenendaal, M., Devereaux, T. P., Hill, J. P., and van den Brink, J. (2011). Resonant inelastic x-ray scattering studies of elementary excitations. *Rev. Mod. Phys.* 83 (2), 705–767. doi:10.1103/RevModPhys.83.705

as part of Programmable Quantum Materials, an Energy Frontier Research Center funded by the U.S. Department of Energy (DOE), Office of Science, Basic Energy Sciences (BES), under award DE-SC0019443. This research uses the beamline 2-ID of the National Synchrotron Light Source II, a DOE Office of Science User Facility operated for the DOE Office of Science by Brookhaven National Laboratory under Contract No. DE-SC0012704. The work of GN was supported by the National Science Foundation (NSF) EPMD program via Grant No. EPMD-2211334. MGe acknowledges the primary support of the U.S. department of energy (DOE), Office of Science, Office of Basic energy Sciences under award number DE-SC0018675. K.S.B acknowledges support by the Air Force Office of Scientific Research under award number FA2386-24-1-4071.

Acknowledgments

We thank Matthias Kuehne for providing access to their Raman spectroscopy equipment and for their assistance during data collection.

Conflict of interest

The authors declare that the research was conducted in the absence of any commercial or financial relationships that could be construed as a potential conflict of interest.

Generative AI statement

The author(s) declare that no Generative AI was used in the creation of this manuscript.

Publisher's note

All claims expressed in this article are solely those of the authors and do not necessarily represent those of their affiliated organizations, or those of the publisher, the editors and the reviewers. Any product that may be evaluated in this article, or claim that may be made by its manufacturer, is not guaranteed or endorsed by the publisher.

Supplementary material

The Supplementary Material for this article can be found online at: <https://www.frontiersin.org/articles/10.3389/femat.2025.1572940/full#supplementary-material>

- Ashraf, A., Mehmood, M., and Janjua, S. A. (2019). Study of ultra-high-vacuum properties of carbon-coated stainless steel beam pipes for high-energy particle accelerators. *Arab. J. Sci. Eng.* 44 (7), 6593–6600. doi:10.1007/s13369-019-03761-6

- Bernasconi, M., Marra, G. L., Benedek, G., Miglio, L., Jouanne, M., Julien, C., et al. (1988). Lattice dynamics of layered MPX₃(M=Mn,Fe,Ni,Zn; X=S,Se) compounds. *Phys. Rev. B* 38 (17), 12089–12099. doi:10.1103/PhysRevB.38.12089

- Breitner, F. A., Jesche, A., Tsurkan, V., and Gegenwart, P. (2023). Thermal decomposition of the Kitaev material α -RuCl₃ and its influence on low-temperature behavior. *Phys. Rev. B* 108 (4), 045103. doi:10.1103/physrevb.108.045103
- Burch, K. S., Mandrus, D., and Park, J.-G. (2018). Magnetism in two-dimensional van der Waals materials. *Nature* 563 (7729), 47–52. doi:10.1038/s41586-018-0631-z
- Calder, R., and Lewin, G. (1967). Reduction of stainless-steel outgassing in ultra-high vacuum. *Br. J. Appl. Phys.* 18 (10), 1459–1472. doi:10.1088/0508-3443/18/10/313
- DiScala, M. F., Staros, D., de la Torre, A., Lopez, A., Wong, D., Schulz, C., et al. (2024). Elucidating the Role of Dimensionality on the Electronic Structure of the Van der Waals Antiferromagnet NiPS₃. *Adv. Phys. Res. n/a* 3 (n/a), 2300096. doi:10.1002/aprx.202300096
- Dvorak, J., Jarrige, I., Bisogni, V., Coburn, S., and Leonhardt, W. (2016). Towards 10 meV resolution: the design of an ultrahigh resolution soft X-ray RIXS spectrometer. *Rev. Sci. Instrum.* 87 (11), 115109. doi:10.1063/1.4964847
- Geiwitz, M., Page, O. R., Marello, T., Nichols, M. E., Kumar, N., Hummel, S., et al. (2024). Graphene multiplexed sensor for point-of-need viral wastewater-based epidemiology. *ACS Appl. Bio Mater.* 7 (7), 4622–4632. doi:10.1021/acsabm.4c00484
- Gong, C., Li, L., Li, Z., Ji, H., Stern, A., Xia, Y., et al. (2017). Discovery of intrinsic ferromagnetism in two-dimensional van der Waals crystals. *Nature* 546 (7657), 265–269. doi:10.1038/nature22060
- Grünleitner, T., Henning, A., Bissolo, M., Zengerle, M., Gregoratti, L., Amati, M., et al. (2022). Real-time investigation of sulfur vacancy generation and passivation in monolayer molybdenum disulfide via *in situ* X-ray photoelectron spectroscopy. *ACS Nano* 16 (12), 20364–20375. doi:10.1021/acsnano.2c06317
- He, W., Shen, Y., Wohlfeld, K., Sears, J., Li, J., Pellicciari, J., et al. (2024). Magnetically propagating Hund's exciton in van der Waals antiferromagnet NiPS₃. *Nat. Commun.* 15 (1), 3496. doi:10.1038/s41467-024-47852-x
- Hellman, F., Hoffmann, A., Tserkovnyak, Y., Beach, G. y. S. D., Fullerton, E. E., Leighton, C., et al. (2017). Interface-induced phenomena in magnetism. *Rev. Mod. Phys.* 89 (2), 025006. doi:10.1103/RevModPhys.89.025006
- Hu, J., Zhang, Y., Law, M., and Wu, R. (2012). First-principles studies of the electronic properties of native and substitutional anionic defects in bulk iron pyrite. *Phys. Rev. B* 85 (8), 085203. doi:10.1103/PhysRevB.85.085203
- Ivanova, T. V., Andres-Penaes, D., Wang, Y., Yan, J., Forbes, D., Ozdemir, S., et al. (2024). Optical contrast analysis of α -RuCl₃ nanoflakes on oxidized silicon wafers. *Appl. Mater.* 12 (7). doi:10.1063/5.0212132
- Kim, D. C., Jeon, D.-Y., Chung, H.-J., Woo, Y. S., Shin, J. K., and Seo, S. (2009). The structural and electrical evolution of graphene by oxygen plasma-induced disorder. *Nanotechnology* 20 (37), 375703. doi:10.1088/0957-4484/20/37/375703
- Kim, K., Lim, S. Y., Lee, J.-U., Lee, S., Kim, T. Y., Park, K., et al. (2019). Suppression of magnetic ordering in XXZ-type antiferromagnetic monolayer NiPS₃. *Nat. Commun.* 10 (1), 345. doi:10.1038/s41467-018-08284-6
- Kim, S., Yuan, B., and Kim, Y.-J. (2022). α -RuCl₃ and other Kitaev materials. *Appl. Mater.* 10 (8), 080903. doi:10.1063/5.0101512
- Kim, S. Y., Kim, T. Y., Sandilands, L. J., Sinn, S., Lee, M.-C., Son, J., et al. (2018). Charge-Spin Correlation in van der Waals Antiferromagnet NiPS₃. *Phys. Rev. Lett.* 120 (13), 136402. doi:10.1103/PhysRevLett.120.136402
- Kuo, C.-T., Neumann, M., Balamurugan, K., Park, H. J., Kang, S., Shiu, H. W., et al. (2016). Exfoliation and Raman Spectroscopic Fingerprint of Few-Layer NiPS₃ Van der Waals Crystals. *Sci. Rep.* 6 (1), 20904. doi:10.1038/srep20904
- Lançon, D., Ewings, R. A., Guidi, T., Formisano, F., and Wildes, A. R. (2018). Magnetic exchange parameters and anisotropy of the quasi-two-dimensional antiferromagnet NiPS₃. *Phys. Rev. B* 98 (13), 134414. doi:10.1103/PhysRevB.98.134414
- Lebert, B. W., Kim, S., Bisogni, V., Jarrige, I., Barbour, A. M., and Kim, Y.-J. (2020). Resonant inelastic x-ray scattering study of α -RuCl₃: a progress report. *J. Phys. Condens. Matter* 32 (14), 144001. doi:10.1088/1361-648X/ab5595
- Li, G., Chen, X., Gan, Y., Li, F., Yan, M., Ye, F., et al. (2019b). Raman spectroscopy evidence for dimerization and Mott collapse in α -RuCl₃ under pressures. *Phys. Rev. Mater.* 3 (2), 023601. doi:10.1103/PhysRevMaterials.3.023601
- Li, Q., Zhou, Q., Shi, L., Chen, Q., and Wang, J. (2019a). Recent advances in oxidation and degradation mechanisms of ultrathin 2D materials under ambient conditions and their passivation strategies. *J. Mater. Chem. A* 7 (9), 4291–4312. doi:10.1039/C8TA10306B
- Liu, Y., Stradins, P., and Wei, S.-H. (2016). Air passivation of chalcogen vacancies in two-dimensional semiconductors. *Angew. Chem.* 128 (3), 977–980. doi:10.1002/ange.201508828
- Lupascu, A., Feng, R., Sandilands, L. J., Nie, Z., Baydina, V., Gu, G., et al. (2012). Structural study of Bi₂Sr₂CaCu₂O₈ exfoliated nanocrystals. *Appl. Phys. Lett.* 101 (22), 223106. doi:10.1063/1.4768234
- Nevshupa, R. A., and de Segovia, J. L. (2002). Outgassing from stainless steel under impact in UHV. *Vacuum* 64 (3), 425–430. doi:10.1016/S0042-207X(01)00345-1
- Park, J.-G. (2016). Opportunities and challenges of 2D magnetic van der Waals materials: Magnetic graphene? *J. Phys. Condens. Matter* 28 (30), 301001. doi:10.1088/0953-8984/28/30/301001
- Rizzo, D. J., Jessen, B. S., Sun, Z., Ruta, F. L., Zhang, J., Yan, J.-Q., et al. (2020). Charge-transfer plasmon polaritons at graphene/ α -RuCl₃ interfaces. *Nano Lett.* 20 (12), 8438–8445. doi:10.1021/acs.nanolett.0c03466
- Saito, R., Hofmann, M., Dresselhaus, G., Jorio, A., and Dresselhaus, M. S. (2011). Raman spectroscopy of graphene and carbon nanotubes. *Adv. Phys.* 60 (3), 413–550. doi:10.1080/00018732.2011.582251
- Sandilands, L. J., Shen, J. X., Chugunov, G. M., Zhao, S. Y. F., Ono, S., Ando, Y., et al. (2010). Stability of exfoliated Bi₂Sr₂DyxCa_{1-x}Cu₂O_{8+ δ} studied by Raman microscopy. *Phys. Rev. B* 82 (6), 064503. doi:10.1103/PhysRevB.82.064503
- Sarikurt, S., Kadioglu, Y., Ersan, F., Vatansver, E., Üzengi Aktürk, O., Yüksel, Y., et al. (2018). Electronic and magnetic properties of monolayer α -RuCl₃: a first-principles and Monte Carlo study. *Phys. Chem. Chem. Phys.* 20 (2), 997–1004. doi:10.1039/C7CP07953B
- Sivadas, N., Okamoto, S., Xu, X., Fennie, C. J., and Xiao, D. (2018). Stacking-dependent magnetism in bilayer CrI₃. *Nano Lett.* 18 (12), 7658–7664. doi:10.1021/acs.nanolett.8b03321
- Suk, J. W., Kitt, A., Magnuson, C. W., Hao, Y., Ahmed, S., An, J., et al. (2011). Transfer of CVD-grown monolayer graphene onto arbitrary substrates. *ACS Nano* 5 (9), 6916–6924. doi:10.1021/nn201207c
- Tang, Y., Su, K., Li, L., Xu, Y., Liu, S., Watanabe, K., et al. (2023). Evidence of frustrated magnetic interactions in a Wigner–Mott insulator. *Nat. Nanotechnol.* 18, 233–237. doi:10.1038/s41565-022-01309-8
- Wang, Y., Balgley, J., Gerber, E., Gray, M., Kumar, N., Lu, X., et al. (2020). Modulation doping via a two-dimensional atomic crystalline acceptor. *Nano Lett.* 20 (12), 8446–8452. doi:10.1021/acs.nanolett.0c03493
- Wildes, A. R., Simonet, V., Ressouche, E., McIntyre, G. J., Avdeev, M., Suard, E., et al. (2015). Magnetic structure of the quasi-two-dimensional antiferromagnet NiPS₃. *Phys. Rev. B* 92 (22), 224408. doi:10.1103/PhysRevB.92.224408
- Wildes, A. R., Stewart, J. R., Le, M. D., Ewings, R. A., Rule, K. C., Deng, G., et al. (2022). Magnetic dynamics of NiPS₃. *Phys. Rev. B* 106 (17), 174422. doi:10.1103/PhysRevB.106.174422
- Wu, Z., Xu, S., Zhou, Y., Guo, Q., Dedkov, Y., and Voloshina, E. (2021). Adsorption of water molecules on pristine and defective NiPX₃ (X: S, Se) monolayers. *Adv. Theory Simulations* 4 (11), 2100182. doi:10.1002/adts.202100182
- Yang, W., Zhu, L., Lu, Y., Henriksen, E., and Yang, L. (2023). Point defects in two-dimensional RuCl₃. *Phys. Rev. Mater.* 7 (6), 064004. doi:10.1103/PhysRevMaterials.7.064004
- Zhou, B., Wang, Y., Osterhoudt, G. B., Lampen-Kelley, P., Mandrus, D., He, R., et al. (2019). Possible structural transformation and enhanced magnetic fluctuations in exfoliated α -RuCl₃. *J. Phys. Chem. Solids* 128, 291–295. doi:10.1016/j.jpcs.2018.01.026